Evaluation of midlatitude clouds in a large-scale high-resolution simulation using CloudSat observations

Thomas J. Greenwald,[1] Yong-Keun Lee,[1] Jason A. Otkin,[1] and Tristan L'Ecuyer[2]

Received 13 November 2009; revised 6 May 2010; accepted 21 May 2010; published 1 October 2010.

[1] The vertical representation, cloud radiative effects (CREs) and radiative heating rates of midlatitude clouds in a large-scale cloud-resolving model simulation were examined using CloudSat observations. Cloud Profiling Radar (CPR) reflectivity profiles were generated from model output and compared objectively to observed CPR profiles by applying cluster analysis to joint histograms of height and reflectivity (H-dBZ). Results of the analysis identified four distinct cloud regimes for both the simulation and observations. Simulated patterns of H-dBZ joint histograms correlated well with observations for all four cloud regimes, i.e., (1) cirrus and low-level cloud, (2) thick cirrus, (3) midlevel convection, and (4) frontal precipitation. The simulation also reproduced well the relative frequency of occurrence of all cloud regimes and their latitudinal dependence. Using a CloudSat radiative flux-heating rate simulator, net CREs at the top of atmosphere, bottom of atmosphere, and for the atmosphere as a whole were found to be in relatively good agreement with observations for cloud regime 1, which occurred over 60% of the time, but were significantly biased for other regimes. While both simulation and observations showed a net column radiative cooling for all cloud regimes, the simulated heating rates indicated much less variation with height. These differences were attributed mainly to errors in the simulated water content profiles and to a lesser extent possible deficiencies in certain ice conversion processes occurring within the model for frontal cloud systems.

Citation: Greenwald, T. J., Y.-K. Lee, J. A. Otkin, and T. L'Ecuyer (2010), Evaluation of midlatitude clouds in a large-scale high-resolution simulation using CloudSat observations, *J. Geophys. Res.*, *115*, D19203, doi:10.1029/2009JD013552.

1. Introduction

[2] The Cloud Profiling Radar (CPR) on CloudSat provides for the first time a means of evaluating globally the detailed vertical structure of clouds simulated by numerical weather prediction (NWP) and general circulation models (GCMs) [*Bodas-Salcedo et al.*, 2008; *Marchand et al.*, 2009]. How well these models distribute clouds vertically and whether they assign reasonably realistic cloud physical properties are crucial, for example, in predictions of precipitation and global warming [*Stephens et al.*, 2002]. Equally important is how clouds distribute their radiative heating vertically in the atmosphere, which has been shown to play a major role in affecting the large-scale circulation and deep convective systems [e.g., *Randall et al.*, 1989; *Grabowski et al.*, 2000].

[3] Recent studies have shown that when compared to CPR observations of joint histograms of height and reflectivity (H-dBZ), global models can reproduce the general cloud structures associated with large-scale circulation features and midlatitude storm tracks [e.g., *Marchand et al.*, 2009]. But depending on the model, they also can exaggerate cloud coverage and low-level precipitation in certain regions, as well as underestimate ice water content in midlatitude storms [*Bodas-Salcedo et al.*, 2008; *Marchand et al.*, 2009]. While these shortcomings likely have a number of different causes, many may be traced to deficiencies in the microphysics and/or planetary boundary layer (PBL) parameterization schemes [e.g., *Otkin and Greenwald*, 2008].

[4] This study also seeks to evaluate model simulated clouds using CPR observations but for a short-term, large-scale, cloud-resolving model simulation that uses a more sophisticated microphysics parameterization than those implemented in GCMs or operational NWP models. Our evaluation approach is similar to earlier studies in that joint histograms of H-dBZ are used; however, the model data are instead matched to the CPR observations in both space and time and compared using cluster analysis to objectively relate similar cloud regimes without prior knowledge of the atmospheric state [*Rossow et al.*, 2005]. Cluster analysis has been used before to evaluate models. For example, *Williams and Tselioudis* [2007] used cluster analysis and International Satellite Cloud Climatology Project observations to test GCMs in the context of cloud response to climate change. However, this study takes the further step of utilizing what is called a CloudSat FLXHR (radiative flux-heating rate) simulator for evaluating not only cloud radiative effects but

[1]Cooperative Institute for Meteorological Satellite Studies, University of Wisconsin, Madison, Wisconsin, USA.
[2]Department of Atmospheric Science, Colorado State University, Fort Collins, Colorado, USA.

0148-0227/10/2009JD013552

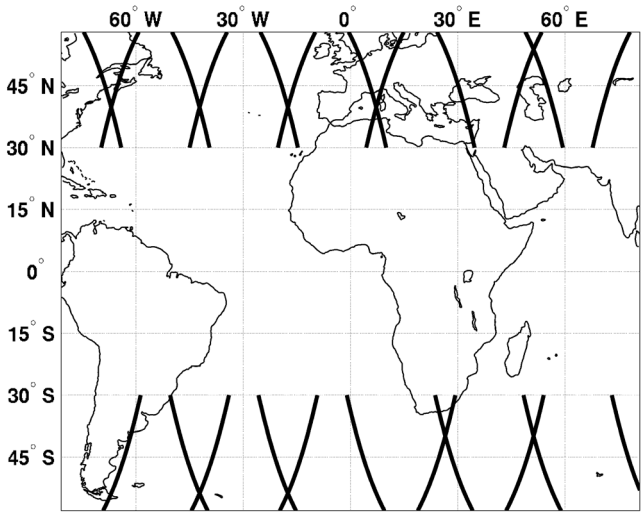

Figure 1. The model simulation domain showing CloudSat tracks for the Cloud Profiling Radar data used in the comparison on 16 August 2006.

also heating rate profiles derived from model output by comparing them to CloudSat 2B-FLXHR products, which provides another perspective in assessing model clouds.

[5] The model simulation evaluated in this study is a unique Weather Research and Forecasting (WRF) model simulation that was generated to help demonstrate the measurement capabilities of the Advanced Baseline Imager to be launched onboard the Geostationary Operational Environmental Satellite (GOES)-R in 2015 [*Otkin et al.*, 2009]. Because of the detailed nature of the comparisons and the lower predictability of cloud formation in areas of tropical convection, the model evaluation is limited to the midlatitudes.

[6] The WRF model simulation and CloudSat observations are summarized in the next two sections. In section 4 the analysis methods are described. Results are given in section 5, followed by the summary and conclusions in section 6.

2. Model Simulation

[7] Version 2.2 of the WRF model [*Skamarock et al.*, 2005] was used to perform a simulation containing a 5950 × 5420 grid point domain with 52 vertical levels that covered the domain depicted in Figure 1 with 3 km horizontal grid spacing. The simulation required approximately 1.5 TB of memory, thus making it among the largest NWP model simulations ever run. This simulation is also unique in that both the horizontal and vertical resolution was comparable to the CPR observations. The largest differences occurred at model levels above 3 km where the grid spacing begins to exceed the CPR range resolution (see section 3). Because a sigma vertical coordinate was used, the vertical spacing increases with height, reaching about 530 m at a height of 10 km.

[8] The model was initialized at 1800 UTC 15 August 2006 with 1° × 1° National Centers for Environmental Prediction Global Data Assimilation System analyses and then run for 30 h. It should be emphasized that cloud observations were not used to initialize the model. Clouds were formed during the 6 h spin-up time. Model data were output every 15 min for 0000–0900 UTC and 1500–2400 UTC and every 5 min for 0900–1500 UTC. More details concerning this simulation are described by *Otkin et al.* [2009].

[9] The microphysical parameterization used in the simulation deserves further discussion. It is a bulk scheme that predicts mixing ratios for five hydrometeor types: cloud water, cloud ice, rain, graupel, and snow, as well as cloud ice number concentration [*Thompson et al.*, 2008]. Although a full two-moment scheme was available for the WRF model, the Thompson et al. scheme was chosen because it provided a significant savings in computational time and was found to perform as well as the two-moment scheme for an extratropical cyclone [*Otkin and Greenwald*, 2008].

[10] The Thompson et al. scheme contains numerous improvements over purely one-moment schemes. For example, it has aspects of sophisticated spectral/bin schemes in terms of the freezing of water droplets and the conversion of cloud ice to snow through the use of lookup tables. The greatest number of improvements, however, is associated with the physical processes and properties of snow. Riming and the accretion of cloud droplets by snow utilize variable collection efficiencies. The snow size distribution consists of a sum of exponential and gamma distributions that depend on ice water content and temperature. Unlike other schemes, snow is assumed as nonspherical with a bulk density inversely proportional to diameter [*Thompson et al.*, 2008].

3. CloudSat Data

[11] CloudSat flies in formation as part of NASA's A-Train carrying the near-nadir-looking CPR operating at 94 GHz [*Stephens et al.*, 2002]. The CPR achieves an effective vertical range resolution of about 240 m and effective footprint size of 1.4 km (across-track) by 2.5 km (along-track). The radar's calibration accuracy is 1.5 dBZ. Over the 1 day period, comparisons were made (0000–2400 UTC 16 August 2006) for a total of over 90,000 CloudSat profiles. Since ground clutter greatly reduces the ability of the CPR to detect clouds near the surface, measurements below 1 km were excluded from the comparisons.

[12] Two Level 2 CloudSat products are used in this study. The Geometrical Profiling (2B-GEOPROF) products provide calibrated reflectivity profiles and cloud mask data. Cloud mask values above 20 were used in the analysis to identify clouds to a high certainty [*Wang and Sassen*, 2007]. The Level 2 flux and heating rate products (2B-FLXHR) offer longwave (LW) and shortwave (SW) radiative flux profiles as well as heating rate profiles that are meant to be consistent with the CPR reflectivities [*L'Ecuyer et al.*, 2008]. These products use the Level 2 cloud water content (2B-CWC) products, temperature, and humidity data from the European Centre for Medium-Range Weather Forecasts, and surface albedo and emissivity data from the International Geosphere-Biosphere Programme as input to a two-stream radiative transfer model for computing broadband fluxes. On the basis of monthly mean comparisons with Clouds and the Earth's Radiant Energy System (CERES) observations averaged over 5° × 5° latitude-longitude areas, *L'Ecuyer et al.* [2008] reported that the outgoing LW and SW radiation RMS errors were 5 and 26 W/m^2, respectively,

with biases of 1 and −5.5 W/m^2, respectively. Biases in the surface LW and SW radiation were significantly larger at −13 and −16 W/m^2, respectively, owing to both the uncertainties in specifying cloud base height in the CERES observations and obtaining information about low clouds within the ground clutter region from CloudSat observations [*L'Ecuyer et al.*, 2008]. Because this study uses instantaneous 2B-FLXHR data, the radiative flux and heating rate errors, particularly the random errors, are expected to be somewhat larger than these estimates.

4. Methods

[13] Simulated CPR reflectivity profiles were derived from WRF model output using an early version of the radar simulator called QuickBeam [*Haynes et al.*, 2007]. This simulator accounts for attenuation of the radar beam by hydrometeors and gases. However, because of the simplifying assumptions used in deriving hydrometeor single scattering properties and the limited size distribution parameters permitted by QuickBeam, significant modifications were made to the software package. To explicitly allow for variations in particle size to affect radar reflectivity, the effective particle diameter D_e, defined as the third moment of the size distribution (proportional to mass) divided by the second moment (proportional to number concentration), was included as an input parameter. Details concerning how D_e is calculated for each hydrometeor type are described by *Thompson et al.* [2008]. Also, because of the large impact of snow on radar reflectivity, D_e for snow was replaced by the explicit size distributions used by the Thompson et al. scheme.

[14] Another important modification to QuickBeam replaced the Mie single scattering calculations for ice spheres with tables based on Discrete Dipole Approximation (DDA) calculations [*Liu*, 2004]. For simplicity, it was assumed that snow particles were shaped as Liu's type-A snowflake, a sector-like particle composed of three intersecting elongated ellipsoids.

[15] While high-resolution-simulated CPR reflectivity profiles are an advantage in that cloud overlap need not be considered, they create other challenges when attempting to match them with nearly coincident CPR observations. For example, simulated cloud features can often be displaced horizontally from their observed location because of translational errors and predictability limits at cloud-resolving scales. Additional difficulties arise from the model's vertical grid spacing being coarser than the CPR observations in the mid-to-upper troposphere.

[16] A relatively simple approach was used in this study to spatially match the simulated and observed reflectivity profiles. To account for small translational errors, simulated CPR profiles were collected within 5 km on either side of the CloudSat track. Vertical resolution disparities were dealt with using the simulated profile levels as a reference and then collecting observations into vertical bins defined by those levels. Figure 1 shows the CloudSat tracks for the region of study over the course of the simulation. Time differences between the model output and the CloudSat overpasses did not exceed 7.5 min.

[17] The collocated simulated and observed reflectivity profiles were represented as joint relative frequency of occurrence histograms of H-dBZ that were classified separately according to a K-Means cluster algorithm, where K is the number of clusters defined a priori [*MacQueen*, 1967]. The algorithm first places centroids of each of the K clusters randomly into the H-dBZ joint histograms that are to be clustered. Each histogram is assigned to the cluster with the closest centroid. The positions of the cluster centroids are then recalculated. These steps are repeated until the sum of the square distances between the centroids and data locations within the joint histograms is minimized.

[18] To ensure statistically meaningful results, the algorithm was applied to joint histograms over 1° latitude sections along the CloudSat track. The resolution of the joint histograms was set as 52 height bins (corresponding to the model grid spacing) and 5 reflectivity bins (10 dBZ intervals). These bin resolutions were selected to take advantage of the high vertical resolution of the simulation and observations but at the same time to provide robust statistical results. Although a finer reflectivity interval of 5 dBZ gave results similar to those using a 10 dBZ interval, the latter was chosen because it produced somewhat better reproducibility in the results from multiple runs of the cluster algorithm. Following the analysis of *Zhang et al.* [2007], only those latitude sections that contained more than 95% cloudy profiles were included in the cluster analysis. Cloudy profiles were determined assuming a CPR minimum level of detectability of −28 dBZ. These criteria yielded a total of 518 one degree latitude sections for the observations and 507 for the simulations.

[19] The final step in applying the cluster analysis was to determine the best value for K. As in the study by *Zhang et al.* [2007] and *Rossow et al.* [2005], this study ran the analysis with different initial guesses of K and then selected the best value objectively using criteria defined by *Rossow et al.* [2005]. The cluster algorithm was applied separately to the simulated and observed data sets for $K = 3$, $K = 4$, and $K = 5$. Analysis of the observations revealed that $K = 4$ satisfied the criteria. As a further step to ensure these results were statistically meaningful, we repeated the analysis on observations for the entire month of August 2006 (not shown). Results indicated that the best value for K was also 4 and that the cluster patterns were nearly indistinguishable from the 1 day analysis (all pattern correlations were above 0.9).

[20] Analysis of the simulated data determined that the best value for K was 4 as well, but not all statistical criteria were met, however. Two of the cluster patterns (1 and 3) exhibited a high intercorrelation of 0.81 (all other pattern correlations were less than 0.46). Despite this problem, there were several reasons to select the $K = 4$ analysis over the $K = 3$ and $K = 5$ results. Not only did the other results violate more of the criteria, but they were also highly dependent on the starting point of the centroid clusters. The $K = 4$ analysis ultimately proved to be more robust since repeated runs of the analysis showed that in about 75% of the cases, initial conditions played little or no role. This also held true for the analysis of the observations. Results representative of these cases for both sets of data are provided in the next section.

[21] An example of the cluster analysis for a portion of one CloudSat track as it passed over a North Atlantic cyclone off the coast of Europe is illustrated in Figure 2.

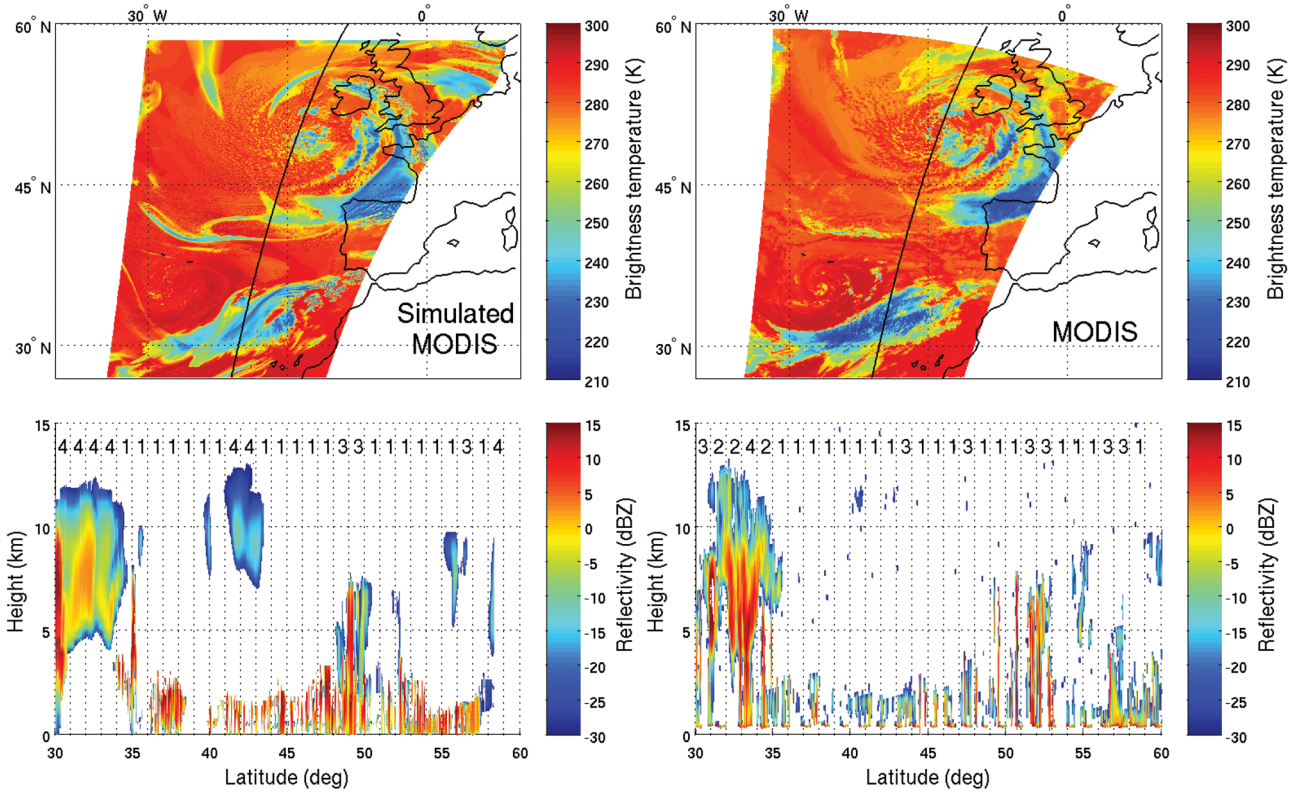

Figure 2. (top) Simulated and observed imagery for MODIS band 31 (11 μm) showing the track of CloudSat. (bottom) Simulated and observed Cloud Profiling Radar cross sections where numbers running across the top of the cross sections represent different cluster centroid numbers from the cluster analysis.

Each of the cluster centroid numbers identified for 1° latitude sections along the track represent similar patterns in H-dBZ space. To obtain the overall pattern for each cluster centroid over all CloudSat tracks, the joint histograms were composited together.

[22] Finally, the CloudSat FLXHR simulator for computing radiative fluxes and heating rates from WRF model output contained the same software infrastructure used to generate the CloudSat 2B-FLXHR products. This was done to ensure that the same set of criteria and forward radiative transfer model used in generating FLXHR products were applied to the simulations. For example, thin high clouds (defined as ice water contents less than 0.01 gm^{-3} or, equivalently, a radar reflectivity threshold of about −30 dBZ) and all clouds in the lowest four range bins were screened in the simulations. In addition, the solar zenith angle was set to 1330 local time, the same assumption used in the generation of the 2B-FLXHR products. However, it should be noted that snow hydrometeors were treated differently in the FLXHR simulator than in QuickBeam in that they followed a single modified gamma distribution rather than the dual distribution used in the Thompson et al. scheme.

5. Results

5.1. H-dBZ Relationships

[23] Figure 3 shows the outcome of the cluster analysis for the WRF model simulation and the CPR observations. Each of the joint histograms for the four cluster centroids represent distinct weather states or cloud regimes [*Rossow et al.*, 2005; *Zhang et al.*, 2007]. Patterns of the first cloud regime (frames labeled CR1 in Figure 3) are consistent with a combination of thin cirrus and boundary layer clouds. These types of cloud systems were by far the most commonly encountered in both the simulation and observations and are associated with partial cloud cover (see Table 1). Differences between the observed and simulated patterns occur mainly in the boundary layer where the simulation exhibited shallower clouds with much larger reflectivities. These differences are reflected in the correlation between the observed and simulated patterns, which was the lowest among the cloud regimes (Table 1). Furthermore, these differences are much larger than either the accuracy of the CPR reflectivities or uncertainties expected from the QuickBeam simulator. Closer examination of the model cloud and precipitation variables suggests these large reflectivities were due mainly to excessive rain.

[24] The second regime (frames labeled CR2 in Figure 3) not only consists primarily of thicker cirrus associated with frontal systems and the intrusion of cirrus from the subtropics but also includes boundary layer clouds. The simulation does a good job of reproducing the joint histogram for this case as evidenced by the high correlation between the simulated and observed patterns (Table 1). As seen in the mean radar reflectivity profiles, the main differences are an overestimation in reflectivity at low levels for the same

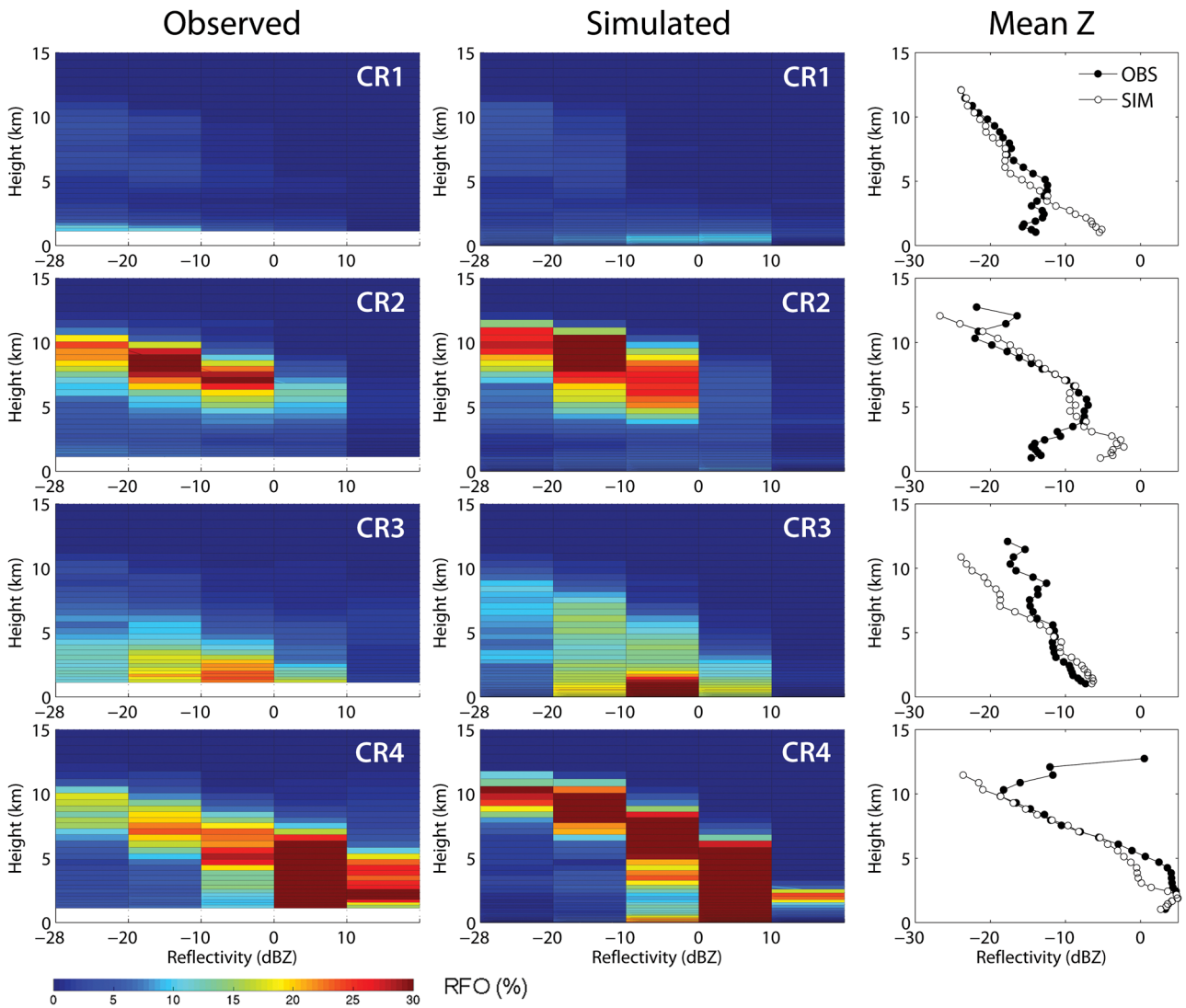

Figure 3. (left) Observed and (middle) simulated joint histograms of height (km) and radar reflectivity (dBZ) for centroids of each of the four cloud regimes (CR1–CR4) in terms of relative frequency of occurrence (RFO). (right) Mean observed and simulated reflectivity (Z) profiles are also shown for each cloud regime.

reason as in cloud regime 1 and an underestimation above 10 km due to the simulation underpredicting cloud ice water content and possibly effective particle size.

[25] The third cloud regime (frames labeled CR3 in Figure 3) may be interpreted as midlevel convection produced by relatively unorganized cloud systems and, hence, contains a mixture of several cloud types. According to the high correlation between the simulated and observed patterns (Table 1), the model appears to have adequately reproduced the histogram pattern for this weather state. However, as noted earlier, the cluster analysis for the simulation revealed that the cluster pattern for this cloud regime was strongly

Table 1. Characteristics of the Observations and Simulation for the Four Cloud Regimes in Terms of Relative Frequency of Occurrence and Cloud Cover[a]

Cloud Regime	Frequency of Observations (%)	Observed Cloud Cover (%)	Frequency of Simulations (%)	Simulated Cloud Cover (%)	Pattern Correlation
1	65.6	47.7	61.5	54.5	0.70
2	14.7	67.8	19.9	86.7	0.90
3	15.1	79.1	14.4	52.6	0.90
4	4.6	78.5	4.1	81.5	0.85

[a]Also shown are the correlations between the observed and simulated joint histogram patterns. All pattern correlations were statistically significant at the 99% level using a t-distribution.

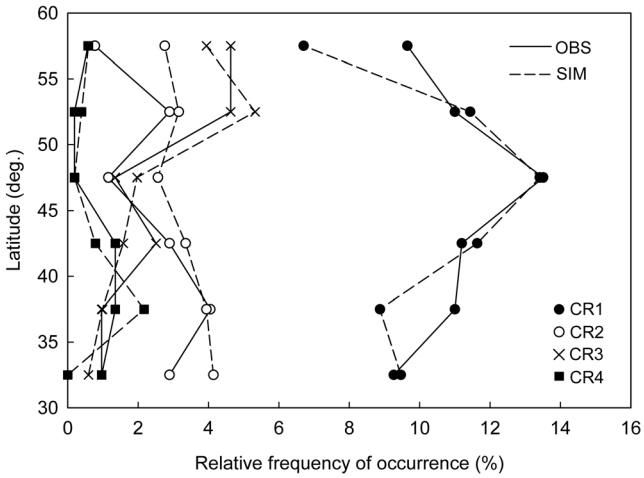

Figure 4. Observed and simulated relative frequency of occurrence (%) of each cloud regime (CR1–CR4) as a function of latitude.

correlated with the pattern of cloud regime 1. This strong correlation is evident in the close resemblance of their mean reflectivity profiles (see Figure 3). Thus, it can be concluded that the joint histograms for these two simulated cloud regimes may actually represent only one regime.

[26] The final cloud regime (frames labeled CR4 in Figure 3) is indicative of frontal precipitation with more vigorous convection and its characteristic trailing cirrus shield. For both the simulations and observations, this regime was the least common but had the greatest cloud cover (Table 1). Overall, the simulation does well in reproducing the structure of these cloud systems. The correlation of this histogram pattern when compared against the observations is also very high (see Table 1). In the lower atmosphere, the maximum radar reflectivities are generally smaller than observed, implying the simulation produced somewhat less intense precipitation, and therefore smaller water content and mean drop size, for these types of cloud systems. The observations also show a large secondary maximum near 12–13 km not seen in the simulations. This maximum was the result of two separate events, one of which had observed reflectivities as large as 20 dBZ, caused by an overshooting cloud top associated with unusually deep convection in a severe storm over Europe. The magnitude of the reflectivity suggests that significant concentrations of large hydrometeors, most likely graupel, were present. It is unlikely, however, that a model could successfully predict both the placement and timing of such an event due to limits in predictability.

[27] Another way to evaluate the model simulation is in terms of how the different cloud regimes are spatially distributed in comparison to the observations [e.g., *Williams and Tselioudis*, 2007]. Although the spatial sampling of the data sets is too sparse to allow for a comparison of the entire geographic area, a comparison with respect to latitude can be made. Figure 4 shows the simulated and observed relative frequency of occurrence for the four cloud regimes as a function of latitude, where the southern and northern latitudes have been combined. Results indicate the simulation accurately captures the latitudinal trends for all cloud regimes.

5.2. Radiative Fluxes and Heating Rates

[28] Further evaluation of the simulation can be done in terms of the effects of the model clouds on the radiation budget. These net cloud radiative effects can be defined at the top of atmosphere (TOA) and bottom of atmosphere (BOA) for the separate LW and SW components as [e.g., *L'Ecuyer et al.*, 2008] $C_{\mathrm{net}} = F_{\uparrow\mathrm{clr}} - F_{\downarrow\mathrm{clr}} - (F_{\downarrow\mathrm{all}} - F_{\downarrow\mathrm{all}})$, where $F_{\uparrow\mathrm{clr}}$ and $F_{\downarrow\mathrm{clr}}$ are the upward and downward flux components for clear-sky, respectively, and $F_{\uparrow\mathrm{all}}$ and $F_{\downarrow\mathrm{all}}$ are the upward and downward flux components for all-sky conditions, respectively. The net cloud radiative effect (CRE) within the atmosphere is the difference between C_{net} at the TOA and C_{net} at the BOA. The total net CRE follows as the sum of C_{net} for the LW and SW components.

[29] Table 2 summarizes the CRE calculations for the simulation and the CloudSat observations for each of the cloud regimes. At the TOA, the simulation tends to underestimate the total net cooling by 8%–61% depending on the cloud regime. However, the simulation results for cloud regimes 1 and 2 agree with the observations if variability is taken into account. The simulated total net results at the BOA also underestimate the total net cooling, with a bias as high as 79%, although after accounting for variability, the results for cloud regime 1 are in agreement with the observations. For the atmosphere as a whole, both the simulation and observations show a net cooling by clouds for cloud regimes 1 and 3 (cirrus over low-level cloud and midlevel convective systems) and a net warming for cloud regimes 2 and 4 (thick cirrus and frontal systems). However, the simulation tends to overestimate the cooling for regimes 1 and 3 and underestimate the warming for regimes 2 and 4. Only for cloud regime 1, however, does the simulation agree with the observations when variability is accounted for. All differences can be traced to low biases (29%–37%) in the LW cloud effect at the TOA caused by too much LW radiation (10–30 Wm^{-2}) being transmitted to space.

[30] Taking the comparisons one step further, the simulated radiative heating rate profiles were evaluated against the observed profiles for each cloud regime (Figure 5). The observations reveal that LW cooling dominates all cloud regimes with the largest net heating rates (> -10 K/d) occurring at cloud tops above 10 km for all cloud regimes except regime 1, where the strongest cooling occurs at 2 km controlled by the radiative influence of low-level clouds over the optically thinner cirrus. Indications of net radiative warming are seen only at the bases of the thick cirrus in regime 2 and at the lowest levels of all regimes.

[31] The simulated heating rates are dominated by LW cooling as well; however, they vary much less with height than the observations. Differences with the observations are most dramatic at mid and low levels for cloud regime 1 and in the upper atmosphere for the other regimes. Although the column mean differences between the simulation and observations are rather small, being less than 0.4 K/d and due in large part to compensating differences, the standard deviation of the differences is actually quite large, ranging from about 2 to 3 K/d for all cloud regimes (see column labeled "original" in Table 3).

Table 2. Mean and Relative Differences of Simulated and Observed Net Longwave, Net Shortwave, and Total Net Cloud Radiative Effects for the Four Cloud Regimes at the Top of Atmosphere, Bottom of Atmosphere, and Within the Atmosphere[a]

	Net LW (Wm^{-2})			Net SW (Wm^{-2})			Total Net (Wm^{-2})		
Cloud Regime	Simulated	Observed	Differences (%)	Simulate	Observed	Differences (%)	Simulate	Observed	Differences (%)
				TOA					
1	19.0 (1.9)	30.0 (4.4)	−37	−103 (10)	−122 (26)	15	−84.0 (10)	−92.0 (21)	8.4
2	52.7 (2.1)	80.4 (8.2)	−34	−79.2 (9.0)	−128 (22)	38	−26.5 (9.0)	−47.6 (18)	44
3	29.7 (1.6)	45.6 (5.1)	−35	−75.5 (7.4)	−146 (23)	48	−45.8 (7.2)	−100.4 (17)	54
4	59.5 (1.8)	83.2 (8.4)	−29	−115 (11)	−226 (32)	49	−55.5 (12)	−142.8 (23)	61
All	30.6 (2.2)	46.7 (3.4)	−34	−93.0 (9.5)	−135 (20)	31	−62.4 (9.4)	−87.9 (20)	29
				BOA					
1	48.1 (2.0)	50.2 (6.9)	−4.1	−114 (11)	−130 (28)	13	−65.9 (11)	−79.8 (22)	18
2	39.0 (1.6)	45.1 (4.8)	−13	−89.8 (9.9)	−138 (24)	35	−50.8 (9.7)	−92.9 (20)	45
3	63.0 (1.2)	65.4 (6.6)	−3.7	−81.8 (8.1)	−156 (24)	48	−18.8 (8.1)	−90.6 (19)	79
4	54.3 (0.6)	63.4 (6.3)	−14	−130 (12)	−243 (34)	47	−75.7 (12)	−179.6 (25)	58
All	49.2 (1.8)	53.1 (2.8)	−7.3	−103 (11)	−144 (22)	28	−53.8 (10)	−90.9 (21)	41
				ATM					
1	−29.1 (2.6)	−20.2 (4.0)	−44	11 (1.6)	8.0 (1.7)	31	−18.1 (3.5)	−12.2 (4.1)	−53
2	13.7 (2.4)	35.3 (2.3)	−61	10.6 (1.3)	10 (1.7)	6.0	24.3 (2.9)	45.3 (3.1)	−46
3	−33.3 (2.1)	−19.8 (2.7)	−68	6.3 (0.9)	10 (1.4)	−37	−27.0 (2.6)	−9.8 (3.2)	−175
4	5.2 (1.5)	19.8 (2.4)	−74	15 (1.4)	17 (1.9)	−13	20.2 (1.6)	36.8 (3.3)	−45
All	−18.6 (2.4)	−6.4 (4.1)	−191	9.9 (1.4)	9.5 (1.7)	4.2	−8.7 (3.1)	3.1 (4.4)	−381

[a]Standard deviations are indicated in parentheses.

[32] To investigate these differences further, both simulated and observed total liquid water content (LWC) and ice water content (IWC) profiles were examined in more detail (Figure 6). Because the strong LW cooling at and above 12 km for cloud regimes 2–4 was found to be caused by just a few observed profiles in each regime with extremely high IWC (in one extreme case exceeding 1 gm^{-3}), these anomalous profiles were subsequently removed from the mean LWC and IWC profiles shown in Figure 6. Statistics of the heating rate differences with these profiles excluded are also shown in Table 3 labeled as "Modified Obs".

[33] Large deviations of the simulated LW cooling from the observations at midlevels for cloud regimes 1 and 3 appear to be caused by a relative peak in the observed IWC that was only weakly reproduced by the simulation. However, it may be possible that the much higher LWC observed at these levels is also contributing to the differences. For regime 1 at low levels, the simulated LW cooling maximum occurs at a slightly lower level since the model generated shallower clouds than observed (Figure 5). The cause of the large differences in the strength of the cooling at these levels is apparently related to the magnitude of the simulated LWC, which is nearly a factor of 2 smaller than observed. The fact that the simulation also produced mean raindrop effective diameters approaching 200 μm may have helped to reduce the broadband IR cloud optical depths and hence the cooling rates.

[34] Other major differences in the magnitude of the cooling rates are evident at about 10 km in cloud regimes 2 and 4. For regime 2, comparison of the IWC profiles in Figure 6 suggests that the amount of ice mass is not the cause of the differences since the simulated IWC is actually slightly larger than observed. For regime 4, the IWC profiles are comparable in magnitude, but the height of the simulated IWC maximum is about 2 km lower than observed, which is consistent with the peak cooling rate at upper levels being about 2 km lower than the height of the observed peak cooling rate.

[35] Remaining differences between the simulation and observations in terms of the magnitude of the LW and net cooling, particularly for regimes 2 and 4, may be unrelated to model deficiencies. For example, errors in the 2B-FLXHR and 2B-CWC products could also contribute to the differences. However, it is useful to explore the possible role that hydrometeor size may play in the comparison. One way that ice particle size produced by the model could be too large is if the microphysics scheme converts too much cloud ice into snow. This is a strong possibility given that the scheme used in the simulation turns on this conversion process when cloud ice particles reach an arbitrary diameter [*Thompson et al.*, 2008]. As seen in Figure 7, the simulation of ice for both cloud regimes 2 and 4 indicates that snow, not cloud ice, is the largest contributor to the ice mass above 10 km, where the particles have diameters ranging from about 100 to 200 μm.

[36] To investigate whether excessive amounts of large ice particles could be the cause of the remaining differences, another set of heating rate calculations using the CloudSat FLXHR simulator were performed whereby all snow and graupel hydrometers were converted to cloud ice by assigning to them the same particle diameters as the cloud ice. It should be emphasized that this experiment is not the same as if the model were run again with these changes because this would affect the fall speed and residence time of the snow and graupel and hence the model simulation. However, this experiment can provide an indication of how sensitive the radiative heating rates are to changes in ice particle size.

[37] Results in Figure 8 show some improvement in the magnitude of LW cooling rates for cloud regimes 2–4 as evidenced by a small reduction in both the mean difference and standard deviation of the column heating rates (see Table 3). Although subtle overall, these improvements are

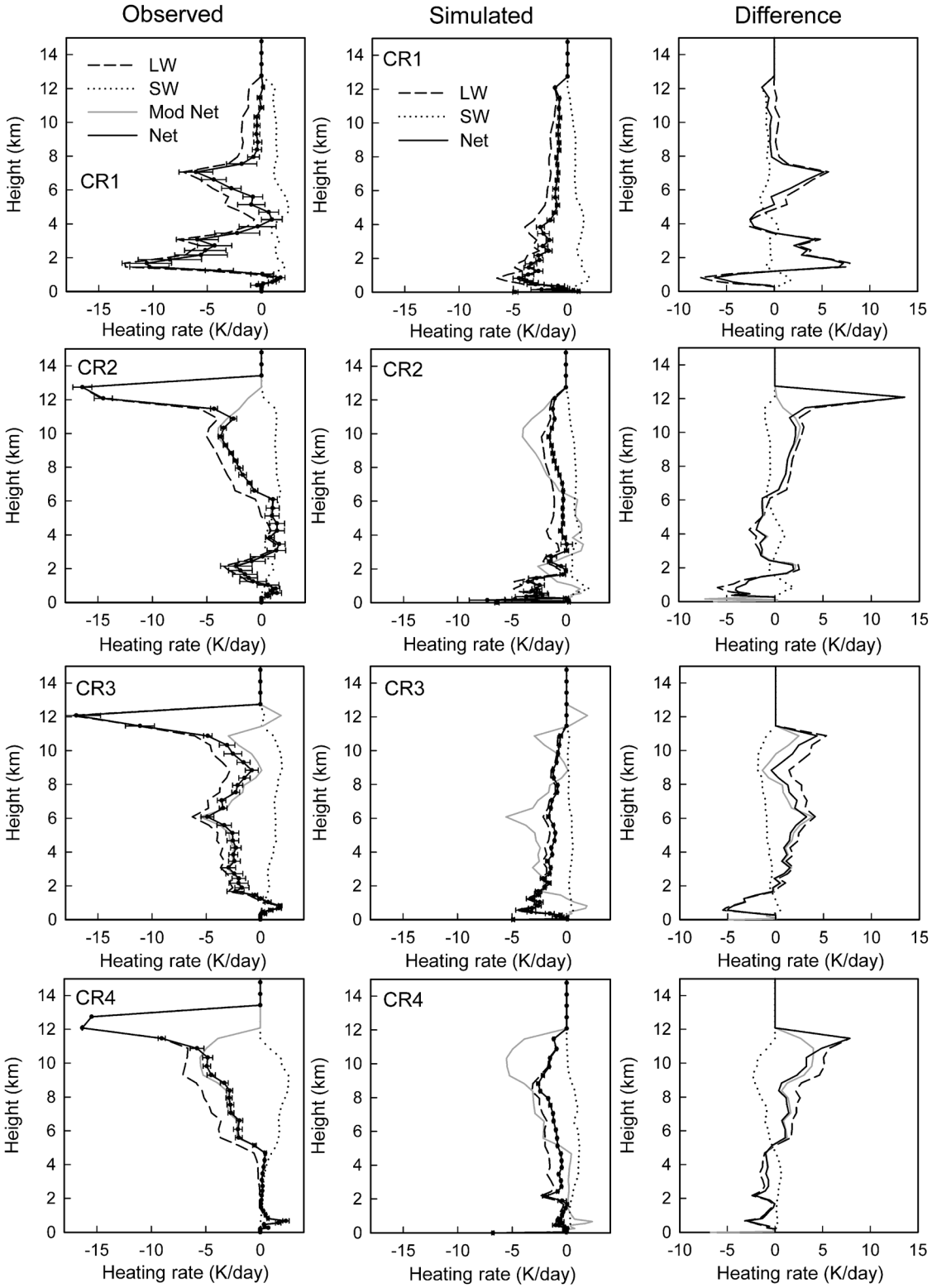

Figure 5. (left) Mean observed and (middle) simulated longwave (LW), shortwave (SW), and net (Net) heating rate (K/d) profiles for each cloud regime (CR1–CR4). Observations with anomalous net heating rate profiles removed are indicated as Mod Net. (right) Differences between simulated and observed profiles.

Table 3. Column Mean Difference and Standard Deviation Between the Simulated and Observed Heating Rate Profiles for Each Cloud Regime[a]

	Original		Modified Obs		Modified Sim	
Cloud Regime	Mean Difference (K/day)	SD (K/d)	Mean Difference (K/d)	SD (K/d)	Mean Difference (K/d)	SD (K/d)
1	0.31	3.3	-	-	0.27	3.3
2	−0.11	3.2	−0.49	2.1	−0.38	1.9
3	0.024	2.4	−0.24	2.3	−0.24	2.2
4	0.33	2.2	0.27	1.8	0.18	1.8

[a]Original refers to unmodified data. Modified observations (Modified Obs) were altered by removing several anomalous profiles, whereas modified simulation (Modified Sim) had graupel and snow particle sizes reduced to those of cloud ice.

most evident for the peak cooling at about 10 km for cloud regime 2, where the shape of the heating profile is captured better, and the peak cooling at 6 km for regime 3. Also seen is a slight improvement in the magnitude of the peak cooling in the upper levels for cloud regime 4. Although this experiment did not bring the simulation into full agreement with the observations, it showed that at least some of the disagreement between the simulated and observed LW cooling rates for cloud regimes associated with deeper convection (i.e., regimes 2–4) could be accounted for by simply reducing the size of the frozen precipitation.

6. Summary and Conclusions

[38] A massive cloud-resolving WRF model simulation was evaluated in terms of its vertical representation of midlatitude clouds and their impact on the radiation budget and radiative heating rates using CloudSat observations. The

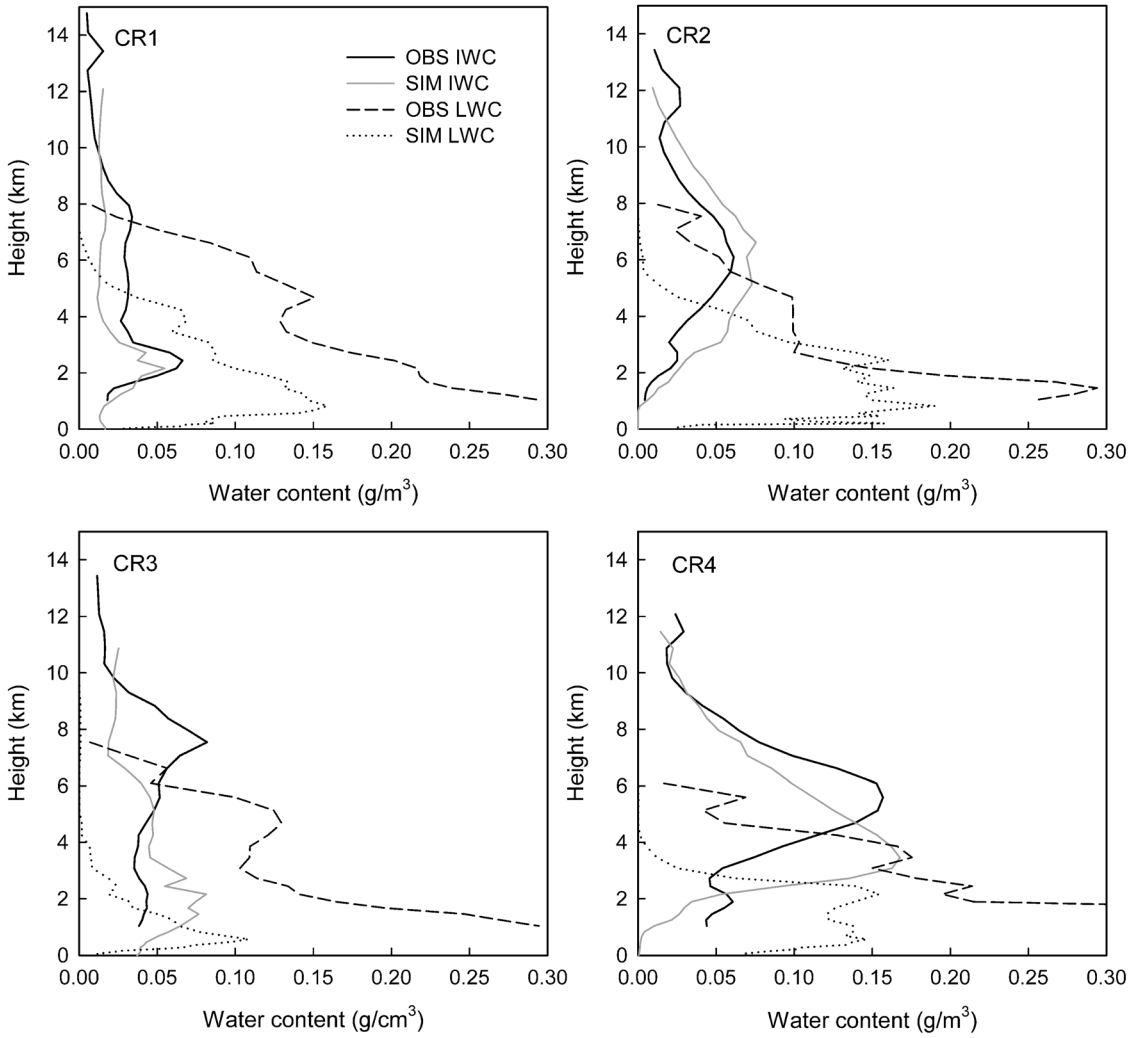

Figure 6. Mean simulated (SIM) and observed (OBS) total ice water content (IWC) and liquid water content (LWC) profiles for each cloud regime (CR).

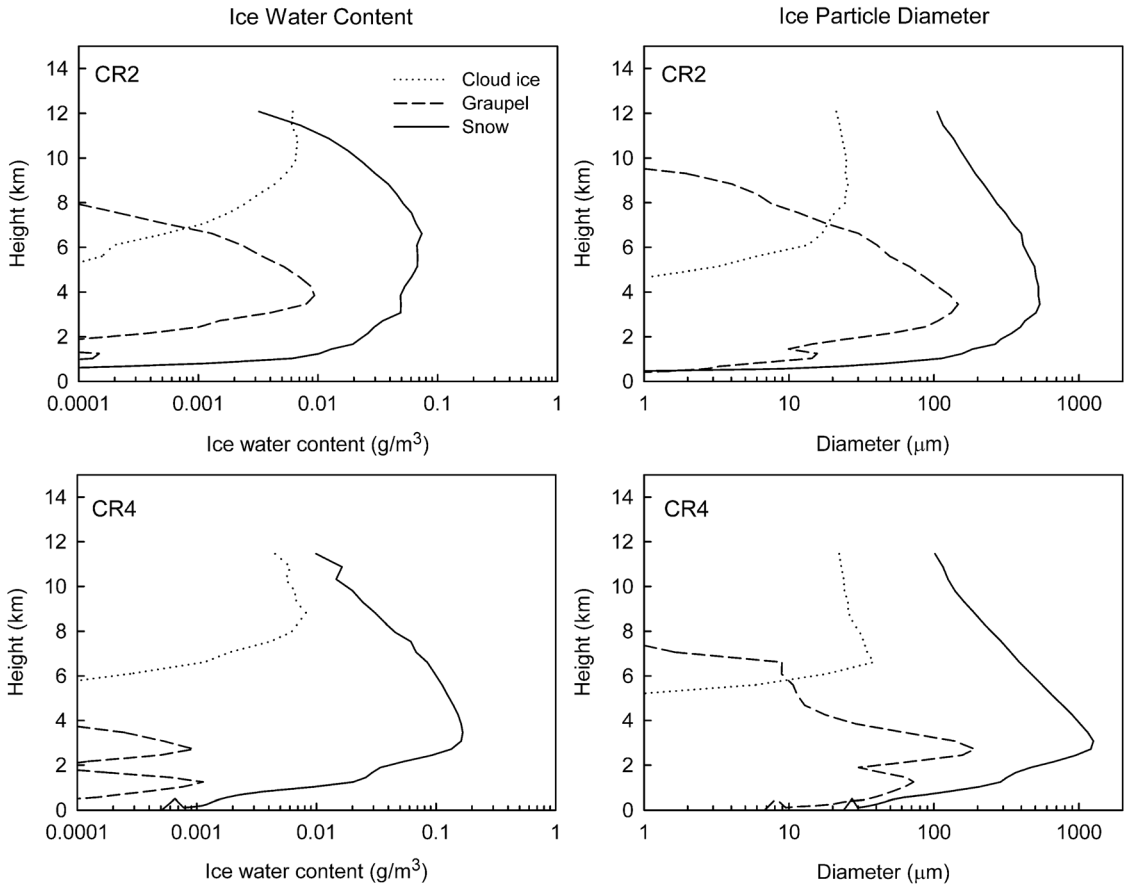

Figure 7. Mean ice water content and ice particle diameter profiles of simulated cloud ice, graupel, and snow for cloud regime 2 (CR2) and 4 (CR4).

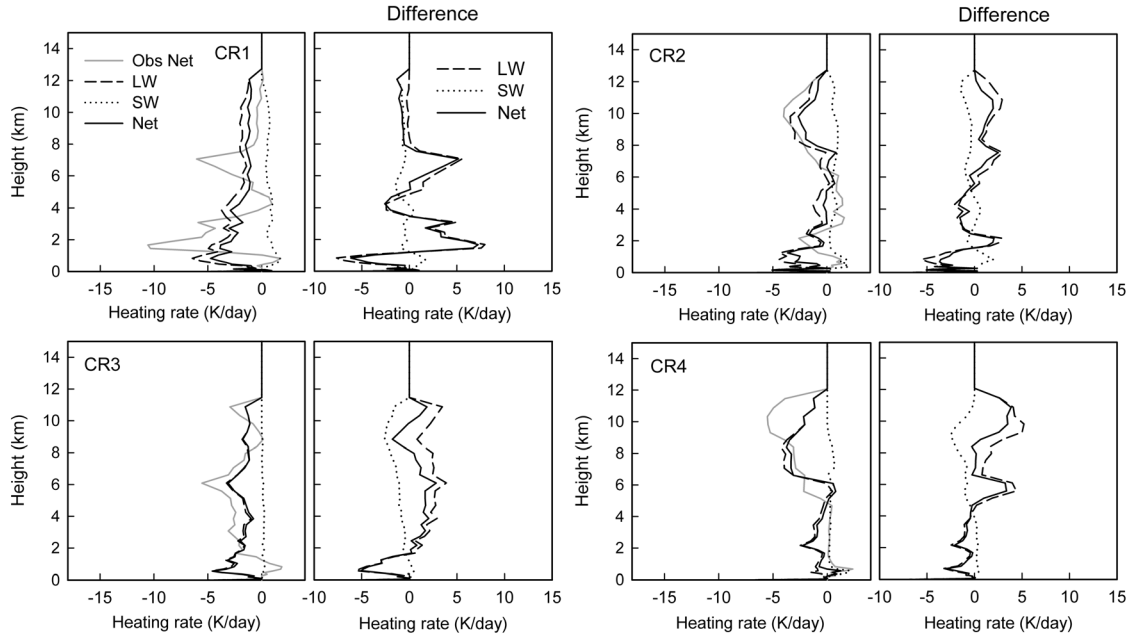

Figure 8. (left) Mean modified simulation of the longwave (LW), shortwave (SW), and net (Net) heating rates (K/d) whereby the diameters of all ice precipitation particles (snow and graupel) are the same as those of cloud ice. Shown for comparison are the mean modified net heating rate observations from Figure 5 (Obs Net). (right) Differences between the modified simulated and modified observed profiles.

evaluation was made by objectively classifying the clouds through cluster analysis. Four different cloud regimes were identified in both the simulation and the observations. Overall, the simulation reproduced well the joint histograms of H-dBZ for all cloud regimes as indicated by statistically significant correlations with the observations. However, pattern correlations were found to be highest for thick cirrus, unorganized midlevel convection, and frontal precipitation. The simulation also reproduced well the relative frequency of occurrence and latitudinal trends of all cloud regimes, where a mixture of cirrus and low-level clouds was the most common regime observed and simulated.

[39] One of the shortcomings of the simulation was that H-dBZ histograms for two of the cloud regimes (thin cirrus with low-level cloud and unorganized midlevel convection) were found to be highly correlated. Whether this is an inherent limitation of the microphysical and/or PBL parameterizations or a result of insufficient statistics in the analysis is unclear. Other weaknesses of this simulation were an overproduction of drizzle and a boundary layer that was too shallow. We suspect this behavior may have been caused by insufficient vertical mixing by the PBL scheme, which prevented latent heat fluxes from being transported vertically. This allowed moisture to build in the boundary layer, thus producing optically thicker clouds with a greater chance of precipitating.

[40] With respect to cloud radiative effects, the simulation performed well for the majority (~60%) of clouds, i.e., a combination of cirrus and low-level clouds. Although differences in the net CRE at the TOA, BOA, and the atmosphere for these clouds when compared against observations ranged from 8% to as high as 53%, all differences were within the variability of the simulated data and observations. However, all simulated clouds displayed positive biases in the net CRE at the TOA and BOA but negative biases for the atmosphere. These negative biases were traced to the simulated clouds losing 10–30 Wm^{-2} more LW radiation to space than observed.

[41] In terms of cloud radiative heating rates, both simulation and observations showed that in all cloud regimes, LW cooling dominated. The simulated heating rates were comparable to the observations in a column sense but varied much less with height than the observations. Although some of these differences could be attributed to differences between the simulated and observed water content profiles, differences in particle size also played a role. For cirrus and low-level clouds (regime 1), the large underestimation of the LW cooling by the simulation at low levels (more than 5 K/d) was due to smaller LWC and relatively large drop sizes caused by an overproduction of drizzle. At least for marine stratiform clouds, such large differences in LW cooling can have a major impact on the vertical motions within the upper regions of the cloud since LW cooling is the dominant mechanism for generating turbulence within this type of cloud [e.g., *Frisch et al.*, 1995]. Perhaps more surprising was the finding that the simulated heating rates could be brought into somewhat better agreement with the observations for cloud regimes associated with deeper convection (i.e., 2–4) by reducing the effective diameters of simulated frozen precipitation, particularly snow, since it was the dominant ice particle type with respect to mass. However, further work is needed using multiple model runs to determine exactly how microphysical changes of this kind will impact model-derived radiative heating rates.

[42] The sensitivity of radiative heating rates to model microphysics as shown in this study highlights the importance of how ice is partitioned in bulk microphysics schemes for these types of weather systems. This partitioning is needed by bulk schemes since they assign ice particles to arbitrary categories. Additionally, these schemes retain only limited aspects of particle growth history. [*Hashino and Tripoli*, 2007]. However, new hybrid bin methods based on first principles that explicitly predict ice particle dimensions (e.g., axis and dendritic arm lengths) and that account for the complete growth history have the potential to provide more realistic depictions of ice particles that may lead to improved radiative heating rates [*Hashino and Tripoli*, 2008]. Although these methods are currently impractical for use in NWP models and GCMs, it may be possible to use the results from these explicit simulations to develop bulk-like parameterizations for improving ice microphysical processes in models.

[43] **Acknowledgments.** Support was provided by the GOES-R Program through NOAA Cooperative Agreement NA06NES4400002. We acknowledge the NASA CloudSat project, which provided CPR observations from the CloudSat Data Processing Center at Colorado State University. We thank Guosheng Liu at Florida State University for the DDA tables and Greg Thompson at the National Center for Atmospheric Research for his assistance with the microphysics scheme. The K-Means clustering algorithm was obtained from the International Satellite Cloud Climatology Project Web site at http://isccp.giss.nasa.gov. We also appreciate the comments of three anonymous reviewers.

References

Bodas-Salcedo, A., M. J. Webb, M. E. Brooks, M. A. Ringer, K. D. Williams, S. F. Milton, and D. R. Wilson (2008), Evaluating cloud systems in the Met Office global forecast model using simulated CloudSat radar reflectivities, *J. Geophys. Res.*, *113*, D00A13, doi:10.1029/2007JD009620.

Frisch, A., D. Lenschow, C. Fairall, W. Schubert, and J. Gibson (1995), Doppler radar measurements of turbulence in marine stratiform cloud during ASTEX, *J. Atmos. Sci.*, *52*, 2800–2808.

Grabowski, W. W., J.-I. Yano, and M. W. Moncrieff (2000), Cloud resolving modeling of tropical circulations driven by large-scale SST gradients, *J. Atmos. Sci.*, *57*, 2022–2039.

Hashino, T., and G. J. Tripoli (2007), The Spectral Ice Habit Prediction System (SHIPS). Part I: Model description and simulation of the vapor deposition process, *J. Atmos. Sci.*, *64*, 2210–2236.

Hashino, T., and G. J. Tripoli (2008), The Spectral Ice Habit Prediction System (SHIPS). Part II: Simulation of nucleation and depositional growth of polycrystals, *J. Atmos. Sci.*, *65*, 3071–3094.

Haynes, J. M., R. T. Marchand, Z. Luo, A. Boda-Salcedo, and G. L. Stephens (2007), A multipurpose radar simulation package: Quickbeam, *Bull. Am. Meteorol. Soc.*, *88*, 1723–1727.

L'Ecuyer, T., N. B. Wood, T. Haladay, G. L. Stephens, and P. W. Stackhouse Jr. (2008), Impact of clouds on atmospheric heating based on the R04 CloudSat fluxes and heating rates data set, *J. Geophys. Res.*, *113*, D00A15, doi:10.1029/2008JD009951.

Liu, G. (2004), Approximation of single scattering properties of ice and snow particles for high microwave frequencies, *J. Atmos. Sci.*, *61*, 2441–2456.

MacQueen, J. B. (1967), Some methods for classification and analysis of multivariate observations, in *Proceedings of 5th Berkeley Symposium on Mathematical Statistics and Probability*, pp. 281–297, Univ. of Calif. Press, Berkeley, Calif.

Marchand, R., J. Haynes, G. G. Mace, T. Ackerman, and G. Stephens (2009), A comparison of simulated cloud radar output from the multiscale modeling framework global climate with CloudSat cloud radar observations, *J. Geophys. Res.*, *114*, D00A20, doi:10.1029/2008JD009790.

Otkin, J. A., and T. J. Greenwald (2008), Comparison of WRF model-simulated and MODIS-derived cloud data, *Mon. Weather Rev.*, *136*, 1957–1970.

Otkin, J. A., T. J. Greenwald, J. Sieglaff, and H.-L. Huang (2009), Validation of a large-scale simulated brightness temperature data set using SEVIRI satellite observations, *J. Appl. Meteorol. Climatol.*, *48*, 1613–1626.

Randall, D. A., D. A. Dazlich Harshvardhan, T. G. Corsetti (1989), Interactions among radiation, convection and large-scale dynamics in a general circulation model, *J. Atmos. Sci.*, *46*, 1943–1970.

Rossow, W. B., G. Tselioudis, A. Polak, and C. Jakob (2005), Tropical climate described as a distribution of weather states indicated by distinct mesoscale cloud property mixtures, *Geophys. Res. Lett.*, *32*, L21812, doi:10.1029/2005GL024584.

Skamarock, W. C., J. B. Klemp, J. Dudhia, D. O. Gill, D. M. Barker, W. Wang, and J. G. Powers (2005), A description of the Advanced Research WRF version 2. *NCAR Tech. Note TN-468+STR*, 88 pp.

Stephens, G. L., et al. (2002), The CloudSat mission and the A-Train: A new dimension of space-based observations of clouds and precipitation, *Bull. Am. Meteorol. Soc.*, *83*, 1771–1790.

Thompson, G., P. R. Field, R. M. Rasmussen, and W. D. Hall (2008), Explicit forecasts of winter precipitation using an improved bulk microphysics scheme. Part II: Implementation of a new snow parameterization, *Mon. Weather Rev.*, *136*, 5095–5115.

Wang, Z., and K. Sassen (2007), Level 2 cloud scenario classification product process description and interface control document, *Coop. Inst. for Res. in the Atmos.*, Colo. State Univ., Fort Collins.

Williams, K. D., and G. Tselioudis (2007), GCM intercomparison of global cloud regimes: present-day evaluation and climate change response, *Clim. Dyn.*, *29*, 231–250, doi:10.1007/s00382-007-0232-2.

Zhang, Y., S. Klein, G. G. Mace, and J. Boyle (2007), Cluster analysis of tropical clouds using CloudSat data, *Geophys. Res. Lett.*, *34*, L12813, doi:10.1029/2007GL029336.

T. J. Greenwald, Y.-K. Lee, and J. A. Otkin, Cooperative Institute for Meteorological Satellite Studies, University of Wisconsin, 1225 West Dayton Street, Madison, WI 53706, USA. (tomg@ssec.wisc.edu)

T. L'Ecuyer, Department of Atmospheric Science, Colorado State University, 200 West Lake St., Fort Collins, CO 80523, USA.